

New Bubble Size Distribution Model for Cryogenic High-speed Cavitating Flow

Yutaka ITO, Kazuhiro TOMITAKA, Takao NAGASAKI
Tokyo Institute of Technology
4259-G3-33, Nagatsuta-cho, Midori-ku, Yokohama, 226-8502, JAPAN
ito@es.titech.ac.jp

Keywords: cavitation, numerical simulation, cryogen, bubble size distribution model

Abstract

A Bubble size distribution model has been developed for the numerical simulation of cryogenic high-speed cavitating flow of the turbo-pumps in the liquid fuel rocket engine. The new model is based on the previous one proposed by the authors, in which the bubble number density was solved as a function of bubble size at each grid point of the calculation domain by means of Eulerian framework with respect to the bubble size coordinate. In the previous model, the growth/decay of bubbles due to pressure difference between bubble and liquid was solved exactly based on Rayleigh-Plesset equation. However, the unsteady heat transfer between liquid and bubble, which controls the evaporation/condensation rate, was approximated by a theoretical solution of unsteady heat conduction under a constant temperature difference. In the present study, the unsteady temperature field in the liquid around a bubble is also solved exactly in order to establish an accurate and efficient numerical simulation code for cavitating flows. The growth/decay of a single bubble and growth of bubbles with nucleation were successfully simulated by the proposed model.

1. Introduction

1.1 Cavitation in a cryogenic turbopump

Flagship rockets of each country employ cryogenic LOX/LH₂ engines which are superior in controllability, thrust and specific impulse. Its turbopumps are required both to operate at a high rotating speed for small size and high pressure output and to be low NPSH for a light fuel tank. Then, it is almost inevitable that cavitation occurs at the turbopumps. As a countermeasure against cavitation, an inducer impeller is set upstream of radial/axial main impellers of the turbopumps. At heavy load operation, however, unsteady cavitation occurs on the inducer impeller and suction performance becomes unstable[1]. Furthermore, cryogenic cavitation has larger thermodynamic effect than water one[2]. Therefore, cavitation of the turbopumps is very complex. Because it is difficult to predict and control cavitation theoretically[3]/ numerically[4], the turbopump is empirically designed based on visible[1] and/or trial[5] tests. There is a possibility that the turbopump can be optimized and improved on by the progress of prediction methods.

Hence high accuracy numerical code is desired for easy optimizing, easy improving on, and reducing the

number of trial manufacturing and experiments. Analyses on cavitation as a basis for developing the code have been proposed by a lot of researchers^[6,7]. Numerical simulation on an inducer by using LES has also been reported by Fujii et al.^[8] In this report, a simplified homogeneous flow model^[9], which assumes that void fraction changes in proportion to the degree of super saturation, was employed as a cavitation model in contrast to the LES model for the accurate simulation of turbulent flow. Results on qualitative tendency such as tip cavitation was obtained, but qualitative results such as discharge pressure didn't agree satisfactorily with experimental results. It seems that the imbalance between the simplified cavitation model and exact LES calculation causes insufficient quantitative accuracy. Therefore it is very important to develop a detailed model of cryogenic cavitation in a high speed turbopump.

1.2 Numerical cavitation model for design of a cryogenic turbopump

To build up a numerical model, it is important to manage both strict modeling of cavitation and reasonable computational time applicable for design. With attention to these points, modeling policies are indicated below.

Gas phase disperses inside liquid phase in a turbopump because of a high speed flow, so the size of each dispersed gas phase is the order of μm to mm , and each shape approaches to spherical. Therefore, a cavitation flow in a turbopump is regarded as a bubbly flow, in other words, gas phase is assumed to be a cloud of spherical bubbles and liquid phase is assumed as a continuum containing bubbles.

In process of bubble growth/decay, Matsumoto et al. reported that incondensable gas plays an important role on bubble phenomena just before collapse[10]. There is a little helium as incondensable gas in a cryogenic turbopump, however, a main purpose of the present study is to evaluate the pump performance, not to analyze microscopic phenomena like erosion. Therefore, incondensable gas is neglected and each bubble is made of pure vapor due to micro size.

In regard to calculation models for the growth/decay of a vapor bubble, the inertia control model and the heat transfer control model are representable. In the former model, the bubble surface temperature is assumed to be equal to that of surrounding liquid, and the change of bubble radius is calculated based on Rayleigh-Plesset equation. In the latter model, the liquid pressure at the bubble surface is assumed to be equal to that of liquid far from

bubble, and the bubble growth is rate controlled by phase change determined by heat transfer in the liquid. The former model is valid when the bubble growth/decay is very rapid even if phase change occurs, and the latter is valid when the bubble growth/decay is very slow. In the present model, both mechanisms are incorporated rigorously in order to deal with various bubble behaviors such as bubble oscillation with phase change.

Heterogeneous bubble nucleation model, which is that bubble nuclei are generated in relation to the degree of super saturation, is employed as the nucleation of cavitation bubble.

It is important to take into account the slip velocity between bubbles and their surrounding liquid because bubbles move in a variable pressure field with external force like centrifugal force. Slip velocity depends on the bubble size, so it is necessary to distinguish bubbles with different sizes between the small bubble just after nucleation and the large bubble well grown. Therefore, bubble size distribution model^[11], whereby bubbles are distinguished based on their mass, is employed. The advection velocities and growth/decay rates of bubbles with size distribution are computed by the model.

In this paper, the above numerical model for cavitation was constructed, and it was applied to growth/decay of cryogenic cavitation bubbles in a liquid at various conditions of super saturation and subcool to verify the usefulness of the model.

2. Bubble growth/decay in a stationary liquid

Bubble radius is calculated by Rayleigh-Plesset equation taking into account the changes of bubble mass and bubble surface temperature due to phase change. Temperature field of liquid phase in the thermal boundary layer around the bubble is calculated simultaneously to determine the phase-change rate and bubble surface temperature. Because the thermal boundary layer varies due to bubble oscillation, spherical numerical grids are laid on thermal boundary layer to solve the temperature distribution.

2.1 Basic equation for bubble growth/decay

One-dimensional spherical coordinate system on a bubble is considered as shown in Fig. 1. r is distance in radial direction, $r=0$ is at the center of a bubble, $r=R$ is at the surface of a bubble, and $r=R_{out}$ is the outer boundary of calculation domain. Because the temperature variation occurs mainly in the region $r < 2R$ in the case of steady heat conduction around a sphere^[12], R_{out} is set at $2R$. Evaporation/condensation rate for a bubble is calculated by temperature gradient at the bubble surface as follows,

$$\partial w / \partial t = \gamma_G = 4\pi R^2 k_L (dT_B / dr)|_{surface} / L \quad (1)$$

Here w denotes mass of vapor bubble, L latent heat of vaporization, and T_B liquid phase temperature

around the bubble. Bubble growth rate, dR/dt , is governed by

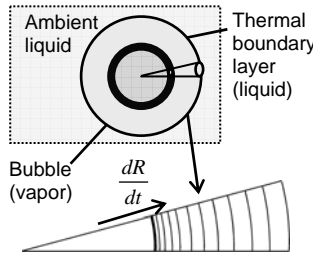


Fig. 1 1D spherical grids for bubble growth/decay

Table 1 Grids for thermal boundary layer

Grid No.	Position
0	1.00000000R
1	1.00751880R
2	1.01503759R
3	1.02757487R
4	1.04848024R
5	1.08333907R
6	1.14146468R
7	1.23838668R
8	1.40000000R
9	1.60000000R
10	1.80000000R
11	2.00000000R

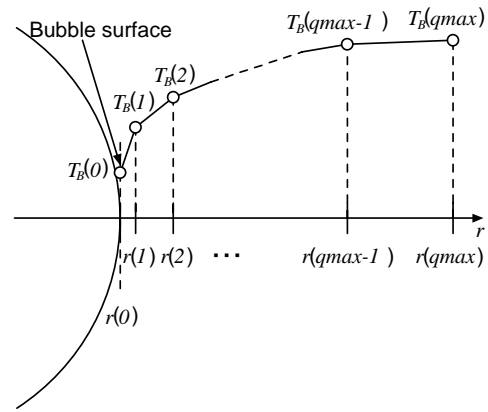


Fig. 2 Temperature distribution in thermal boundary layer

$$P_G - P_L = \frac{2\sigma_s}{R} + \rho_L R \frac{d^2 R}{dt^2} + \frac{3}{2} \rho_L \left(\frac{dR}{dt} \right)^2 + \frac{4\mu_L}{R} \frac{dR}{dt} \quad (2)$$

from Rayleigh-Plesset equation. By saturation condition, bubble temperature T_G and pressure P_G are obtained from bubble density ρ_G .

$$\rho_G = 3w / (4\pi R^3) \quad (3)$$

$$T_G = T_{sat}(\rho_G) \quad (4)$$

$$P_G = P_{sat}(\rho_G) \quad (5)$$

Local radial velocity c at r is derived from the surface velocity $c|_{surface}$.

$$c = c_{surface} R^2 / r^2 = \{dR/dt - \gamma_G / (4\pi R^2 \rho_L)\} R^2 / r^2 \quad (6)$$

Temperature distribution T_B is calculated by Lagrangian differential equation on the system moving at local speed c .

$$\frac{DT_B}{Dt} = \frac{k_L}{\rho_L C_{pL}} \frac{1}{r^2} \frac{d}{dr} \left(r^2 \frac{dT_B}{dr} \right) \quad (7)$$

2.2 Analytical method for bubble growth/decay

Firstly, the mass rate of phase change, γ_G , is calculated by using spatial 2nd order discretized form of eq. (1).

$$\gamma_G = 4\pi(R^{old})^2 k_L / L [-\Delta_1 / \{\Delta_2(\Delta_1 + \Delta_2)\} T_B^{old}(2) \quad (8)$$

+ $(\Delta_1 + \Delta_2) / \{\Delta_1 \Delta_2\} T_B^{old}(1) - (2\Delta_1 + \Delta_2) / \{\Delta_1(\Delta_1 + \Delta_2)\} T_G^{old}$]
where, $T_B(q)$, $r(q)$ are values at grid point q , where q is index of grid as shown in Fig. 2. Grid interval $\Delta_1 = r^{old}(1) - R^{old}$, and $\Delta_2 = r^{old}(2) - r^{old}(1)$. Positive γ_G means evaporation.

The bubble mass at the new time step, w , is obtained by explicit time marching of eq. (1) with time interval Δt_R .

$$w = w^{old} + \gamma_G \Delta t_R \quad (9)$$

where superscript, *old*, denotes previous time step.

Bubble radius, R , is calculated from dR/dt by the following procedure based on eq. (2).

$$\begin{aligned} \text{nth stage: } (dR/dt)^n &= (dR/dt)^{old} + f(R^{an}, (dR/dt)^{an}, b^n \Delta t_R) \\ R^n &= R^{old} + (dR/dt)^n b^n \Delta t_R \end{aligned} \quad (10)$$

where

$$\begin{aligned} f(R^{an}, (dR/dt)^{an}, b^n \Delta t_R) &= [P_G^{old} - P_L - 2\sigma_s / R^{an} \quad (11) \\ &- 3/2 \rho_L \{(dR/dt)^{an}\}^2 - 4\mu_L / R^{an} (dR/dt)^{an}] b^n \Delta t_R / (\rho_L R^{an}) \end{aligned}$$

Applying Jameson's factors, $a_n = (old, 1, 2, 3)$, $b_n = (1/3, 4/15, 5/9, 1)$ for $n=1$ to 4, eq. (10) becomes 4 stages Runge-Kutta method with temporal 2nd order accuracy. New values of ρ_G , T_G and P_G are obtained by eqs. (3) to (5). T_B is calculated by implicit time marching using spatial 2nd order and temporal 1st order discretized equation derived from eq. (7).

$$\begin{aligned} \frac{T_B(q) - T_B^{old}(q)}{\Delta t_R} &= \frac{k_L}{\rho_L C p_L} \left\{ \frac{2}{r(q)} \left(\frac{dT_B}{dr} \right)_q + \left(\frac{d^2 T_B}{dr^2} \right)_q \right\} \\ (dT_B/dr)_q &= \{g_{11} T_B(q-1) + g_{12} T_B(q) + g_{13} T_B(q+1)\} \quad (12) \\ (d^2 T_B/dr^2)_q &= \{g_{21} T_B(q-1) + g_{22} T_B(q) + g_{23} T_B(q+1)\} \\ g_{11} &= -\Delta_2 / \{\Delta_1(\Delta_1 + \Delta_2)\}, \quad g_{12} = (\Delta_2 - \Delta_1) / (\Delta_1 \Delta_2), \\ g_{13} &= \Delta_1 / \{\Delta_2(\Delta_1 + \Delta_2)\}, \quad g_{21} = 2 / \{\Delta_1(\Delta_1 + \Delta_2)\}, \\ g_{22} &= -2 / (\Delta_1 \Delta_2), \quad g_{23} = 2 / \{\Delta_2(\Delta_1 + \Delta_2)\} \\ \Delta_1 &= r(q) - r(q-1), \quad \Delta_2 = r(q) - r(q+1) \end{aligned}$$

Then, the following equation is obtained.

$$\begin{aligned} a(q) T_B(q-1) + b(q) T_B(q) + c(q) T_B(q+1) &= d(q) \quad (13) \\ a(q) &= -k_L / (\rho_L C p_L) \{g_{11} / r(q) + g_{12}\}, \\ b(q) &= 1 / \Delta t_R - k_L / (\rho_L C p_L) \{g_{12} / r(q) + g_{22}\} \\ c(q) &= -k_L / (\rho_L C p_L) \{g_{13} / r(q) + g_{23}\}, \quad d(q) = T_B^{old}(q) / \Delta t_R \end{aligned}$$

The above equation is organized into a matrix form.

$$\begin{pmatrix} 1 & & & & 0 \\ a(1) & b(1) & c(1) & & \\ & a(2) & b(2) & \ddots & \\ & & & b(q_{max}-1) & c(q_{max}-1) \\ 0 & & & & 1 \end{pmatrix} \begin{pmatrix} T_B(0) \\ T_B(1) \\ T_B(2) \\ \vdots \\ T_B(q_{max}) \end{pmatrix} = (T_G, d(1), d(2), d(3), \dots, d(q_{max}-1), T_L)^{transpose} \quad (14)$$

Under $T_B(0) = T_G$ and $T_B(q_{max}) = T_L$, T_B is solved by diagonalizing the factor's matrix. Due to implicit method, limitation of time interval can be ignored for T_B calculation. However, limitation of time interval is imposed due to bubble oscillation, and the time

interval is determined by using natural frequency for vapor bubble by Prosperetti^[13] as follows.

$$\Delta t_R = 1 / (f_{na} C_R) \quad (15)$$

$$f_{na} = 1 / 2\pi \sqrt{(3\kappa_p R_{equ} P_{sat} - 2\sigma_s) / (\rho_L R_{equ}^3)}$$

where, the constant, C_R , are set to 20, and the equivalent bubble radius R_{equ} is given by a representative bubble size of the calculation. Index κ_p approaches to specific heat ratio γ_{SHR} for high frequency. In case of $dt_B/dr|_{surface} > 0$ and large Δt_R , some bubbles unphysically become super critical bubbles, $T_G > \text{critical temperature } T_c$, and dissolve into liquid. So, temperature change ΔT_G during Δt_R is limited to be smaller than 10% T_c .

$$\begin{aligned} \Delta t_R &= \gamma_{G, Limit} L / \{4\pi R^2 k_L (dT_B/dr)|_{surface}\} \quad (16) \\ \gamma_{G, Limit} &= 4\pi R^3 \{\rho_{sat}(T_G + 0.1T_c) - \rho_G^{old}\} / 3 \end{aligned}$$

Because T_B is calculated by Lagrangian framework based on eq. (7), the new value of T_B for each old grid point corresponds to the temperature at the distance $c(q)\Delta t_R$ away from position of old grid point. Therefore T_B at the new grid points, as indicated in Table 2, is interpolated by cubic spline approximation.

2.3 Result of a single bubble growth/decay in a stationary liquid at constant pressure

The growth/decay behavior of a bubble in liquid nitrogen is shown in Fig. 3. A bubble with $R_0 = 10^{-6}$ m and $T_{G0} = 0.75T_c$ is put into the liquid at $t=0$. Liquid temperature and pressure far from the bubble are assumed to be constant with respect to time. Liquid pressure is set to balanced pressure with initial bubble pressure and surface tension of the bubble. Liquid temperature is parametrically changed from superheat to subcool conditions. Three kind of numerical grids for the thermal boundary layer are employed as followings.

Type1: $1=0.0010R$ and 1000 grid points (uniform),
Type2: $1=0.0075R$ and 133 grid points (uniform),
Type3: $1=0.0075R$ and 11 grid points (non-uniform, see Table 1).

Thermal boundary layer with thickness 10 % R_0 and linear temperature profile is assumed as an initial condition in order to give the same initial temperature profile independent of grid interval. Because results by type 1 and type2 agree well in all cases, it is verified that results by type 1 are rigorous. Calculation load, i.e. computational time, by type 3 is smaller by a factor of 90 compared with by type 1. The difference between the results by type 3 and rigorous ones by type1 is small (5% error at maximum), so it is verified that type 3 grids is enough to obtain bubble behaviors.

Figure 4 shows results under the same condition as Fig. 3, except that liquid temperature is set to equilibrium temperature with initial bubble temperature and liquid pressure is parametrically changed from 50% to 1000% saturation pressure of equilibrium temperature. In case of superheat

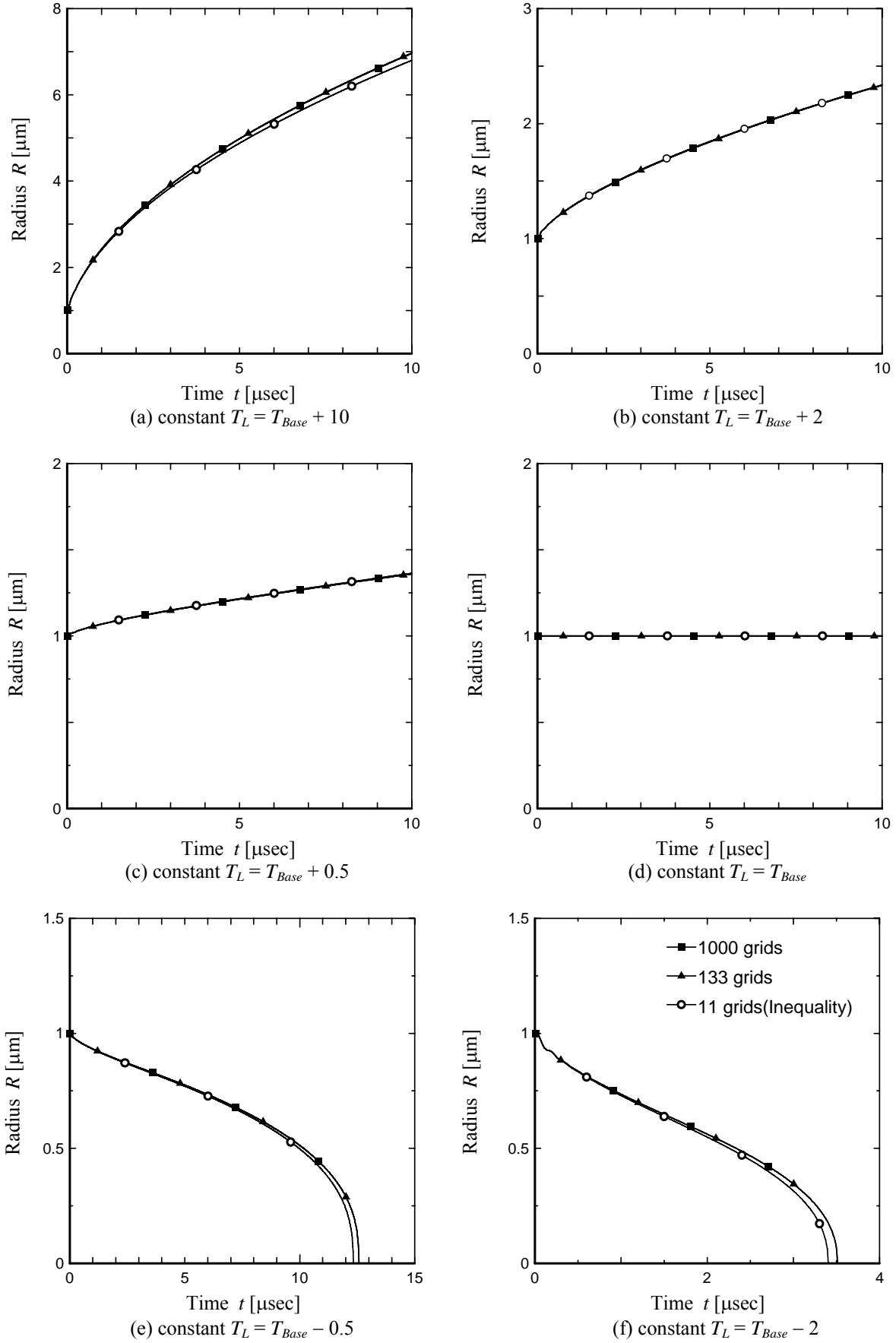


Fig. 3 Comparison of results by using various numerical grids in case of constant T_L, P_L
 $\text{LN}_2, T_{Base} = 0.75T_c, P_{Base} = P_{sat}(T_{Base}), \Delta t = 10^{-12}, P_L = P_{Base} - 2\sigma/R_0, T_{G0} = T_{Base}, P_{G0} = P_{Base}$

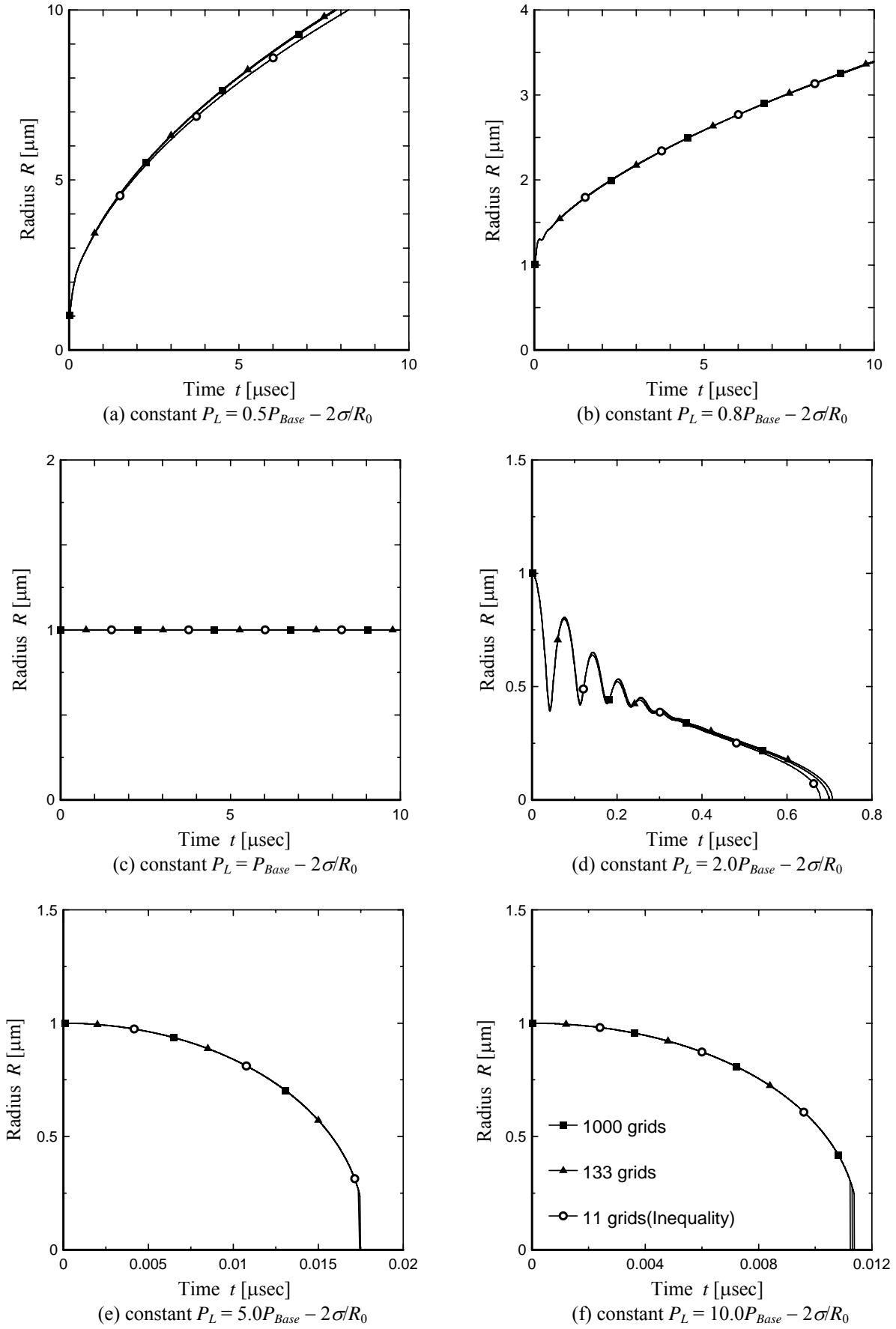


Fig. 4 Comparison of results by using various numerical grids in case of constant T_L , P_L
 LN_2 , $T_{Base} = 0.75T_c$, $P_{Base} = P_{sat}(T_{Base})$, $\Delta t = 10^{-12}$, $T_L = T_{Base}$, $T_{G0} = T_{Base}$, $P_{G0} = P_{Base}$

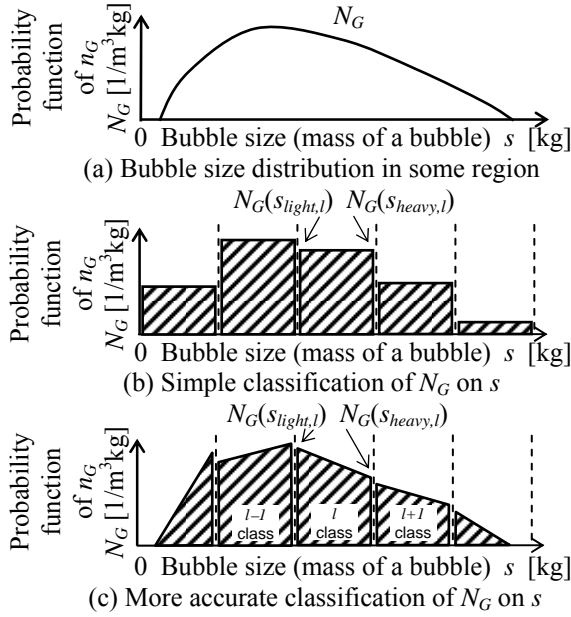


Fig. 5 Bubble size distribution model

conditions, i.e. smaller liquid pressure, the initial bubble growth is in condition of inertia control. In some cases oscillation occurs in the early period as seen in Fig. 4(b) by the following reason: Due to the initial rapid growth, evaporation is insufficient to support bubble growth, so the bubble pressure reduces and the bubble shrinks momentarily because inertia wins pressure difference between the bubble and liquid. After that the bubble pressure recovers and the bubble regrows. The amplitude gradually decreases and the bubble behavior shifts to moderate growth controlled by heat transfer. On the other hand in case of subcool conditions, the bubble just after insertion shrinks in condition of inertia control. Due to the rapid decrease of bubble radius, condensation is insufficient to keep bubble decay, so the bubble pressure rises and the bubble rebounds momentarily because inertia wins pressure difference between the bubble and liquid. After that the bubble pressure reduces and the bubble shrinks again. The amplitude of oscillation gradually decreases and the bubble behavior shifts to moderate decay controlled by heat transfer. Because the agreement between type 3 and the rigorous one (type1) is almost satisfactory, it is verified that the present numerical model is appropriate to simulate bubble behavior even in the case of growth/decay with oscillation.

3. Bubble growth/decay by using BSD model

Bubble size distribution model whereby bubbles are distinguished based on their mass, advection velocity are calculated, and growth/decay rates are computed using Eulerian framework, is employed.

3.1 Basic equation for bubble growth/decay by BSD

In order to employ bubble mass w as the measure of bubble size for Eulerian framework, an independent variable s is introduced.

$$s = 4\pi R^3 \rho_G / 3 \quad (17)$$

Namely, bubble mass axis s is defined in addition to the spatial axes x, y, z . It should be noted that the definition of s is the same as w , but w is dependent variable. An example of bubble distribution in a certain volume is shown in Fig. 5(a) by probability density function N_G of bubble number density n_G . as a function of s . Basic equations can be written as conservative equations of N_G .

$$\partial N_G / \partial t + \partial (N_G \gamma_G) / \partial s = \Pi_G \delta(s - w_0) \quad (18)$$

$$\partial (s N_G) / \partial t + \partial (s N_G \gamma_G) / \partial s = s \Pi_G \delta(s - w_0) + N_G \gamma_G \quad (19)$$

$$\partial (R N_G) / \partial t + \partial (R N_G \gamma_G) / \partial s = R_0 \Pi_G \delta(s - w_0) \quad (20)$$

$$\partial (\dot{R} N_G) / \partial t + \partial (\dot{R} N_G \gamma_G) / \partial s = \dot{R}_0 \Pi_G \delta(s - w_0) \quad (21)$$

$$\partial (T_B N_G) / \partial t + \partial (T_B N_G \gamma_G) / \partial s = T_L \Pi_G \delta(s - w_0) \quad (22)$$

In these equations, Π_G denotes nucleation rate (number of generated bubbles due to nucleation per unit volume per unit time), w_0 mass of one nucleated bubble, and γ_G evaporation (condensation for negative value) rate per one bubble of size s . Because the mass of one bubble increase with time due to the evaporation, bubbles move at speed γ_G in s direction. In the same way, $s N_G$, $R(s)$, $\dot{R}(s)$ and $T_B(r, s)$ also move in s direction.

3.2 Discretization of basic equation with respect to the bubble mass axis for BSD

N_G is discretized with respect to coordinate s , and conservative values $n_{G,l}$, $m_{G,l}$ are defined for the discretized region (sub region) in the s coordinate.

$$n_{G,l} \equiv \int_{s_{light,l}}^{s_{heavy,l}} N_G ds \quad (23)$$

$$m_{G,l} \equiv \int_{s_{light,l}}^{s_{heavy,l}} (s N_G) ds = s_{average,l} n_{G,l} = w_{l,l} n_{G,l} \quad (24)$$

Conservation equation for $n_{G,l}$, $m_{G,l}$ are derived from eqs. (18)(19).

$$\partial n_{G,l} / \partial t + [N_G \gamma_G]_{s_{light,l}}^{s_{heavy,l}} = \Pi_G - \Phi_{G,l} \quad (25)$$

$$\partial m_{G,l} / \partial t + [s N_G \gamma_G]_{s_{light,l}}^{s_{heavy,l}} = w_0 \Pi_G - \Psi_{G,l} + n_{G,l} \gamma_{G,l} \quad (26)$$

In order to solve new values of $n_{G,l}$, $m_{G,l}$ by using eqs. (25)(26), the profile of N_G in the sub region must be assumed, as shown in Fig. 5(b)(c), because the boundary values of each sub section are required in the 2nd term of left-hand side of eqs. (25)(26). It should be noted that the hatched area of the l th sub region in Fig. 5(b)(c) corresponds to $n_{G,l}$ based on eq. (23). A uniform profile shown in Fig. 5(b) is simple, however, the profile is determined uniquely only by $n_{G,l}$ obtained from eq. (25), and $m_{G,l}$ cannot satisfies

eqs. (24) and (26) simultaneously. On the other hand, by using a linear profile shown in Fig. 5(c), the profile is determined uniquely to satisfy eqs. (23)-(26). Therefore a linear profile is employed. The linear distribution has 3 patterns. Pattern 1 is the case of $(s_{light,l} + 2s_{heavy,l})/3 \leq w_l$, Pattern 2 is the case of $(2s_{light,l} + s_{heavy,l})/3 \leq w_l < (s_{light,l} + 2s_{heavy,l})/3$ and Pattern 3 is the case of $w_l < (s_{light,l} + 2s_{heavy,l})/3$.

$$\begin{aligned} \text{Pattern 1: } s_{min} &= 3w_l - 2s_{heavy,l}, s_{max} = s_{heavy,l} \\ (s_{light,l} + 2s_{heavy,l})/3 &\leq w_l < s_{heavy,l} \\ N_{Gw}(s_{light,l}) &= 0 \\ N_{Gw}(s_{heavy,l}) &= 2n_{G,l} / \{3(s_{heavy,l} - w_l)\} \end{aligned} \quad (27)$$

$$\begin{aligned} \text{Pattern 2: } s_{min} &= s_{light,l}, s_{max} = s_{heavy,l}, \Delta s = s_{heavy,l} - s_{light,l} \\ (2s_{light,l} + s_{heavy,l})/3 &< w_l < (s_{light,l} + 2s_{heavy,l})/3 \\ N_G(s_{light,l}) &= 2n_{G,l}(3w_l - 2s_{light,l} - s_{heavy,l}) / \Delta s^2 \\ N_G(s_{heavy,l}) &= 2n_{G,l}(2s_{heavy,l} + s_{light,l} - 3w_l) / \Delta s^2 \end{aligned} \quad (28)$$

$$\begin{aligned} \text{Pattern 3: } s_{min} &= s_{light,l}, s_{max} = 3w_l - 2s_{light,l} \\ s_{light,l} &< w_l \leq (2s_{light,l} + s_{heavy,l})/3 \\ N_{Gw}(s_{light,l}) &= 2n_{G,l} / \{3(w_l - s_{light,l})\} \\ N_{Gw}(s_{heavy,l}) &= 0 \end{aligned} \quad (29)$$

In case of growth and $w_l \leq (s_{light,l} + 2s_{heavy,l})/3$, distribution is pattern 3 and there is no flux into class $l+1$ because of $N_G(s_{heavy,l})=0$. After bubble growth, in case that w_l becomes larger than $(s_{light,l} + 2s_{heavy,l})/3$, distribution is pattern 2 and flux into class $l+1$ exists because $N_G(s_{heavy,l})$ gets a positive value. Namely, bubbles grow into heavier class only in case of patterns 1 and 2, and bubbles decay into lighter class only in case of patterns 2 and 3. This function prevents numerical diffusion on interclass growth/decay of bubbles.

3.3 Calculation method for bubble growth/decay by BSD

Figure 6 shows a flowchart of bubble growth/decay calculation by using BSD.

Firstly, time intervals Δt_F , Δt_R , Δt_S , Δt_P are determined, where Δt_F is for the flow calculations, Δt_R for the calculations of Rayleigh-Plesset eq. and thermal boundary layer at each class at each grid, Δt_S for the interclass calculations in s direction (time marching of bubble size distribution) at each grid, Δt_P for the liquid temperature and pressure calculations at each grid. They have relationship of $\Delta t_F \geq \Delta t_P \geq \Delta t_S \geq \Delta t_R$. Δt_F is decided by CFL condition. Δt_P is decided by Eq. (15) and $C_R=5$. Δt_S is decided by the following stability condition for Eq. (26).

$$w_l + |\gamma_{G,l}| \Delta t_S \leq s_{heavy,l+1}, w_l - |\gamma_{G,l}| \Delta t_S \geq s_{light,l-1} \quad (30)$$

Because $\gamma_{G,l}$ is unknown before calculation shown in chapter 2, conceivable maximum $\gamma_{G,l}$ is assumed and Δt_S is estimated. $\gamma_{G,l}$ is proportional to $dT_B/dr|_{surface}$

and R_l squared as shown in Eq. (1). In case of decay, because both $dT_B/dr|_{surface}$ and R_l are decreasing during Δt_S , initial $\gamma_{G,l}$ can be regarded as maximum.

$$\Delta t_S \leq (w_l - s_{light,l-1}) / |\gamma_{G,l}| \quad (31)$$

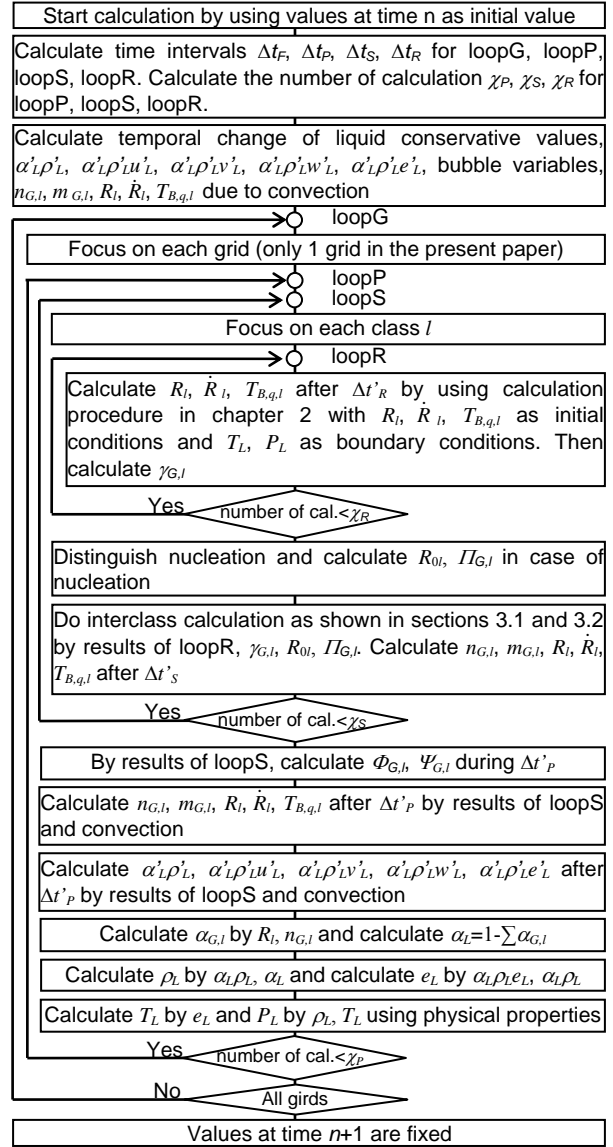


Fig. 6 Flowchart for BSD

In case of growth, both $dT_B/dr|_{surface}$ and R_l are increasing during Δt_S . Conceivable maximum $R_{max,l}$ is $\sqrt[3]{3s_{heavy,l+1}/4\pi\rho_G}$ at bubble mass $s_{heavy,l+1}$ from stable condition of Eq. (20). $dT_B/dr|_{surface}$ becomes larger because of increasing R_l , but it becomes smaller because of thermal diffusion. For $\gamma_{Gmax,l}$ calculation, it is enough to consider $dT_B/dr|_{surface}$ only in case of increasing temperature gradient. New grid interval $\Delta r'_{0,l}$ is calculated from $\Delta r_{0,l} = r_{1,l} - r_{0,l}$ by using Eq. (6) wherein the evaporation term in the right hand side is ignored.

$$r'_{0,l} = R_{0,l} + dR_l/dt \Delta t_S \leq R_{max,l} \quad (32)$$

$$r'_{1,l} = R_{0,l} + \Delta r_{0,l} + dR_l/dt \{ R_{0,l}^2 / (R_{0,l} + \Delta r_{0,l})^2 \} \Delta t_S \quad (33)$$

$$\Delta r'_{0,l} = \Delta r_{0,l} - dR_l/dt \Delta r_{0,l} (2R_{0,l} + \Delta r_{0,l}) \Delta t_s / (R_{0,l} + \Delta r_{0,l})^2 \quad (34)$$

Because $dR_l/dt \leq (R_{max,l} - R_{0,l})/\Delta t_s$ is obtained from Eq. (32), eq. (34) is rewritten as

$$\Delta r'_{0,l} / \Delta r_{0,l} \leq 1 - (R_{max,l} - R_{0,l})(2R_{0,l} + \Delta r_{0,l}) / (R_{0,l} + \Delta r_{0,l})^2 \quad (35)$$

Temperature gradient is inversely proportional to grid interval as indicated by eq. (1), so $\gamma_{Gmax,l}$ is given by

$$\gamma_{Gmax,l} / \gamma_{G,l} = (R_{max,l} - R_{0,l})^2 / (\Delta r'_{0,l} / \Delta r_{0,l}) \quad (36)$$

From eqs.(30) and (36), the stability condition of Δt_s is expressed by

$$\Delta t_s \leq \frac{s_{heavy,l+1} - w_l}{|\gamma_{G,l}|} \left(1 - \frac{(R_{max,l} - R_{0,l})(2R_{0,l} + \Delta r_{0,l})}{(R_{0,l} + \Delta r_{0,l})^2} \right) \left(\frac{R_{max,l}}{R_{0,l}} \right)^2 \quad (37)$$

$\Delta t'_p$, $\Delta t'_s$, $\Delta t'_R$ employed in the practical calculation are decided as

$$\text{Integer: } \chi_P = \text{ceiling}(\Delta t_F / \Delta t_P), \Delta t'_P = \Delta t_F / \chi_P \quad (38)$$

$$\text{Integer: } \chi_S = \text{ceiling}(\Delta t'_P / \Delta t_S), \Delta t'_S = \Delta t'_P / \chi_S \quad (39)$$

$$\text{Integer: } \chi_R = \text{ceiling}(\Delta t'_S / \Delta t_R), \Delta t'_R = \Delta t'_S / \chi_R \quad (40)$$

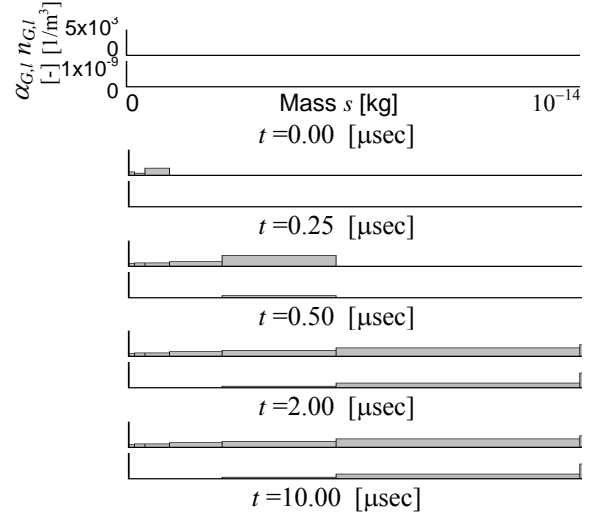


Fig. 7 Continuous nucleation into the constant temperature and pressure liquid by BSD

LN₂, $T_{Base} = 0.75T_c$, $P_{Base} = P_{sat}(T_{Base})$, $\Delta t = 10^{-10}$
 $T_L = T_{Base}$, $T_{G0} = T_{Base}$, $P_L = P_{Base} - 2\sigma/R_0$, $P_{G0} = P_{Base}$
 $s_1 = 10^{-16}$ ($s_i = 10^{(i-49)/3}$) x 9 classes, $R_0 = 0.5\mu m$

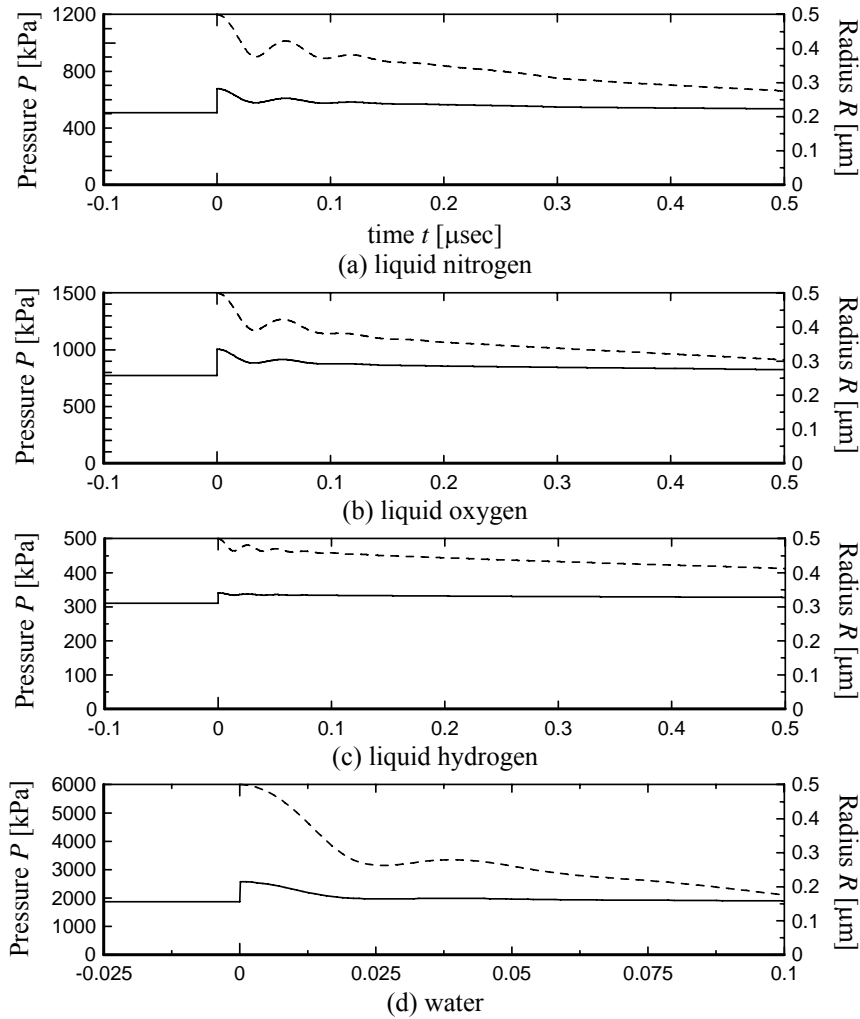


Fig. 8 Temporal change of R_l , P_L after bubble insertion at $t = 0$ into liquid at constant volume by BSD

LN₂, $T_{Base} = 0.75T_c$, $P_{Base} = P_{sat}(T_{Base})$, $T_{L0} = T_{G0} = T_{Base}$, $P_{L0} = P_{Base} - 2\sigma/R_0$, $P_{G0} = P_{Base}$, $\Delta t = 10^{-11}$ [sec]
 $s_1 = 10^{-18}$ ($s_i = 10^{(i-55)/3}$) x 7 classes, $R_0 = 0.5\mu m \times 10^{15}$ 個/ m^3 x (once at first)

Here, $\text{ceiling}(a)$ is minimum integer equal to or greater than real number a .

By using time intervals described above, flow field and bubble distribution are solved. Although the complete calculation procedure for cavitating flows is shown in Fig. 6, only one grid without flow is treated in this paper.

Therefore, the calculation of liquid conservative values and bubble variables due to convection is omitted, and as the first step of the present calculation, Rayleigh-Plesset equation and thermal boundary layer are solved χ_R times to get R_l , \dot{R}_l , $T_{B,q,l}$ and $\gamma_{G,l}$ for each bubble size class l as described in chapter 2.

As the second step, the interclass calculation, that is, calculation of bubble distribution due to the bubble growth across the bubble class, are made χ_S times by $\Delta t'_s$. By this calculation based on eqs. (25)(26), $n_{G,l}$ and $m_{G,l}$ are obtained. In case of super heat condition, Π_G is calculated beforehand. In addition, R_l , \dot{R}_l and $T_{B,q,l}$ are corrected taking into account the bubble growth/decay across the bubble class based on Eqs. (20)(21)(22). Further, number and mass of collapse bubbles, $\Phi_{G,l}$ and $\Psi_{G,l}$, are calculated.

In the case of full calculation, the results of interclass calculation are corrected by results of convection.

Finally, $T_{G,l}$, $\alpha_{G,l}$ and α_l are calculated by

$$T_{G,l} = T_{\text{sat}}(\rho_{G,l}) = T_{\text{sat}}\{3m_{G,l}/(4\pi R_l^3 n_{G,l})\} \quad (41)$$

$$\alpha_{G,l} = 4\pi R_l^3 n_{G,l}/3 = m_{G,l}/\rho_{\text{sat}}(T_{G,l}) \quad (42)$$

$$\sum_{l=1}^{l_{\text{max}}} \alpha_{G,l} + \alpha_L = 1 \quad (43)$$

3.4 Continuous nucleation in a stationary liquid at constant pressure

Figure 7 shows temporal change of $n_{G,l}$ and $\alpha_{G,l}$ distributions in case that a nitrogen bubble with $R_0=0.5\mu\text{m}$ and $T_{G0}=0.75T_c$ is put at every 10^{-10} sec into liquid nitrogen at constant temperature and pressure. Bubble nuclei gradually grow into heavier bubbles. As indicated by comparing results of $2\mu\text{sec}$ and $10\mu\text{sec}$, steady state is attained after $2\mu\text{sec}$ in the bubble class less 10^{-14} kg because the bubble inflow from lighter class and the bubble outflow into heavier class becomes balanced.

3.5 Temporal change of bubble radius and liquid pressure after a nucleation in a stationary liquid at constant volume

Figure 8 shows temporal change of R_l and P_L in case that 10^{15} bubbles with $R_0=0.5\times 10^{-6}\text{m}$ and $T_{G0}=0.75T_c$ are put at $t=0$ into liquid in 1 m^3 closed vessel. Calculations are made for nitrogen, oxygen, hydrogen and water. Liquid pressure steeply increases just after the bubbles insertion

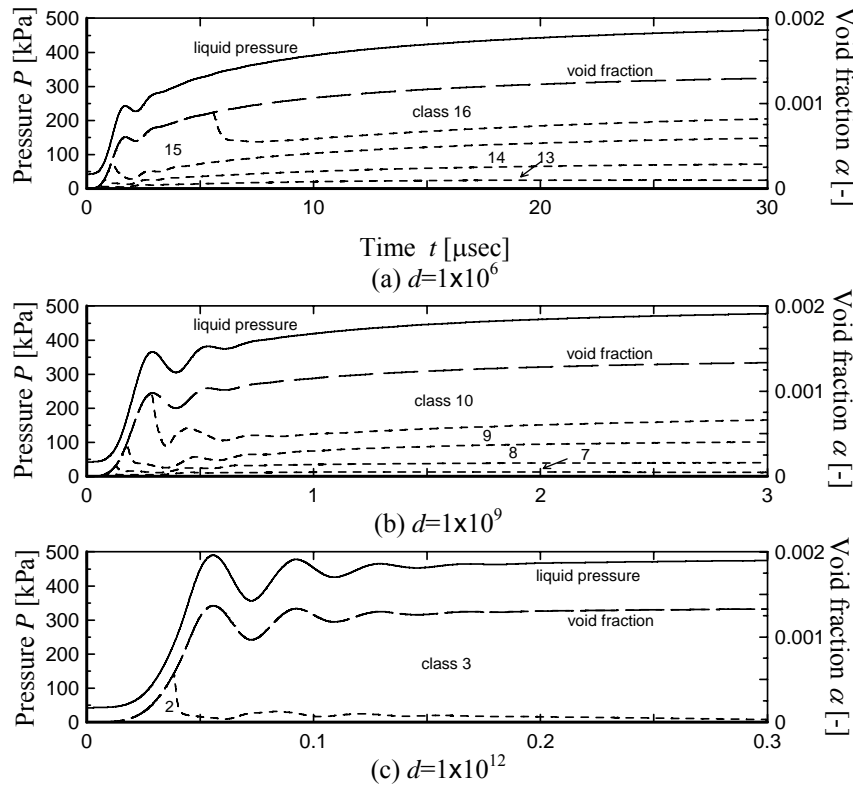


Fig. 9 Temporal change of cumulative $\alpha_{G,l}$, P_L by using heterogeneous nucleation theory in superheat liquid at constant volume by BSD
 LN_2 , $T_{\text{Base}}=0.75T_c$, $P_{\text{Base}}=P_{\text{sat}}(T_{\text{Base}})$, $T_{L0}=T_{G0}=T_{\text{Base}}$, $P_{L0}=0.1P_{\text{Base}}-2\sigma/R_0$, $P_{G0}=P_{\text{Base}}$, $\Delta t=10^{-11}[\text{sec}]$
 $s_l=10^{-18}$ ($s_l=10^{(i-55)/3}$) $\times 31$ classes, $\theta=175.0$ [$\phi=1.08\times 10^{-5}$]

due to compression. Therefore, bubbles are also compressed by liquid, and their radius decreases. Resilience acts in case of radius less than equilibrium value, but inertia gets the bubbles smaller than the equilibrium radius. After the minimum radius, the bubbles expand, and inertia get them larger than the equilibrium radius inversely. These oscillations are gradually attenuated into balanced pressure and equilibrium radius by effect of viscosity.

4. Bubble nucleation according to the heterogeneous nucleation theory

The nucleation rate of bubble nuclei with radius $R_0=2\sigma_s/(P_{sat}-P_L)$ are given by heterogeneous nucleation theory^[14].

$$\Pi_G = d \sqrt{\frac{3\sigma_s}{\pi m_m}} \exp\left(-\frac{16\pi\sigma_s^3}{3} \frac{\phi}{kT_L (P_{sat} - P_L)^2}\right) \quad (44)$$

$$\phi = (2 + 3\cos\theta - \cos^3\theta)/4 \quad (45)$$

where d is the number density of heterogeneous nucleation sites in the liquid, and θ is contact angle of liquid to the heterogeneous nucleation site. The superheat limit of liquid is controlled by the parameter ϕ . Π_G is used in Eqs. (25)(26). Dependent variables like R_l are averaged based on $n_{G,l}$ and Π_G for the bubble class which include R_0 .

4.1 Bubble nucleation in a stationary liquid at constant volume: Effect of nuclei density d

Figure 9 shows temporal change of cumulative $\alpha_{G,l}$ and P_L by changing number density of bubble seeding nuclei d . Terminal values of α_G and P_L are the same for different values of d . However, nuclei grow into large bubbles slowly in case of small d . On the other hand in case of large d , nuclei grow into small bubbles quickly and overshoots and oscillations occur due to large inertia.

5. Conclusion

A numerical code was developed by using a bubble size distribution model for the cavitating flow in turbopump of cryogenic rocket engine.

Firstly, the bubble growth/decay calculations employ two rigorous methods, that is, both Rayleigh-Plesset equation and the heat conduction equation for the thermal boundary layer around the bubble are solved numerically, and the mass rate of evaporation/condensation is evaluated exactly by the solution of temperature field. Secondly, the above calculations are combined with the bubble size distribution model which deals with the bubbles composed various sizes with Eulerian framework with respect to bubble size coordinate. It is verified that the present model can predict complex behaviors of bubble efficiently such as growth/decay with oscillation, and growth of bubbles with continuous or

instantaneous bubble generation. Finally, in order to apply practical cavitating flow, it is confirmed that the present model predicts successfully the behavior of bubbles with heterogeneous nucleation and transient processes into an equilibrium state in a fixed volume corresponding to the calculation of one computational cell in full numerical simulations.

References

- 1) Kamijo, K.: Cavitating flow of inducer, *Turbo machinery*, Vol. 26, No. 3, 1998, pp.161-168, in Japanese.
- 2) Stahl, H., et al.: Thermodynamic aspects of cavitation in centrifugal pumps, *ASME Paper*, No. 55-A-136, 1955, pp. 1691-1693.
- 3) Tsujimoto, Y. et al.: Nonlinear calculation of rotating cavitation in inducers, *Journal of Fluids Engineering, Transactions of the ASME*, Vol. 118, No. 3, 1996, pp. 589-596.
- 4) Shimagaki, M. et al. : Effect of the casing configurations on the internal flow in rocket pump inducer, *Proceedings of AIAA/ASME/SAE/ASEE 42nd Joint Propulsion Conference*, Vol. 9, 2006, pp. 7223-7231.
- 5) Kamijo, K. and Yoshida, M.: Experimental study of LE-7 LOX pump inducer, *Transactions of the Japan Society of Mechanical Engineers, Part B*, Vol. 57, No. 44, 1991, pp. 4023-4028, in Japanese.
- 6) Delale, C. F., et al.: Quasi-one-dimensional steady-state cavitating nozzle flow, *Journal of Fluid Mechanics*, Vol. 427, 2001, pp.167-204.
- 7) Y. Tamura, et al.: Physical modeling and solution algorithm for cavitating simulations, *AIAA paper* 2001-2652, 2001.
- 8) K. Fujii, et al.: Numerical Simulation of Rocket Engine Internal Flows, *Annual Report of the Earth Simulator Center*, April 2005 - March 2006, 2006, pp.161-165.
- 9) Okita, K. and Kajishima, T.: Numerical simulation of unsteady cavitating flows around a hydrofoil, *Transactions of the Japan Society of Mechanical Engineers, Part B*, Vol. 68, No. 667, 2002, pp.637-644, in Japanese.
- 10) Y. Matsumoto, et al.: Influence of internal phenomena on gas bubble motion, *JSME International Journal, Part B*, Vol.37, No.2, 1994, pp. 288-296.
- 11) Ito, Y.: *Method of cavitation analysis, program of cavitation analysis, and their storage and analyzer*, Japanese patent, Kokai-number 2005-222339, 2004
- 12) R. B. Bird, et al.: *Transport Phenomena*, Wiley, New York, 2001
- 13) Prosperetti, A.: The thermal behaviour of oscillating gas bubbles, *Journal of Fluid Mechanics*, Vol. 222, 1991, pp.587-616.
- 14) Van P. Carey: *Liquid-vapor phase-change phenomena*, Hemisphere, Washington, 1992

Nomenclature

c : Velocity in r direction [m/sec]
 d : Number density of seeding nuclei [$1/m^3$]
 e : Internal energy [J/kg]
 f_{na} : Natural frequency [Hz]
 k_B : Boltzmann constant = 1.38×10^{-23} [J/K]
 l : Grid number in s direction [–]
 m : Bubble mass per unit volume [kg/m^3]
 m_m : Mass of a molecule [kg]
 n : Bubble number density [$1/m^3$]
 P : Pressure [Pa]
 q : Grid number in r direction [–]
 r : Axis in radial direction of bubble [m]
 R : Radius / Averaged radius in a class [m]
 \dot{R} : Temporal change of R [m/sec]
 s : Axis in direction of bubble mass [kg]
 T : Temperature [K]
 w : Bubble mass / Averaged bubble mass in a class [kg]

α : Void fraction [–]
 γ : Evaporation/condensation rate per a bubble [kg/sec]
 Δt : Time interval [sec]
 θ : Contact angle between nucleus and impurity [°]
 Π : Number density of nuclei [$1/m^3$ sec]
 ρ : Density [kg/sec]
 σ_s : Surface tension coefficient [N/m]
 Φ : Rate of bubble collapse [$1/m^3$ sec]
 ϕ : Index of limitation of superheat [–]
 χ : Number of calculation [–]
 Ψ : Mass rate of bubble collapse [kg/m^3 sec]

Superscript / subscript

0 : Initial condition
 B : Thermal boundary layer around bubble
 G : Vapor phase
 L : Liquid phase
 old : Value before 1 timestep